Journal of
Materials Chemistry A

PAPER

View Article Online
View Journal | View Issue

Cite this: *J. Mater. Chem. A*, 2026, **14**, 17569

A universal model for energy level alignment at interfaces of hole-collecting monolayers in p-i-n perovskite solar cells

Aruto Akatsuka,[a] Minh Anh Truong,[b] Atsushi Wakamiya,[b] Gaurav Kapil,[c] Shuzi Hayase[c] and Hiroyuki Yoshida*[ad]

Received 11th June 2025
Accepted 11th March 2026

DOI: 10.1039/d5ta04749h

rsc.li/materials-a

Hole-collecting monolayers (HCMs) have attracted considerable attention in p-i-n (inverted structure) perovskite solar cells. Although HCMs exhibit superior performance compared with widely used polymers, there is confusion regarding energy level alignment at electrode/HCM/perovskite interfaces, which is crucial for achieving hole collection efficiency through HCM. In this work, ultraviolet photoelectron spectroscopy, low-energy inverse photoelectron spectroscopy, and metastable atom electron spectroscopy are employed to investigate prototypical carbazole-based HCMs: 2PACz, MeO-2PACz, and 3PATAT-C3. Based on precisely determined energy parameters, we propose a universal model for energy level alignment at electrode/HCM/perovskite interfaces. The key feature of this model is the application of the semiconductor heterojunction theory, in which both the HCM and perovskite layers are treated as semiconductors, whereas the electrode/HCM interface is treated in terms of interface dipole formation. The model is further tested on HCMs beyond the carbazole-based types, confirming its universal applicability. The origins of the key energy parameters in the model are analyzed to establish design rules for HCM development. Particular attention is given to the oft-overlooked work function of the transparent conductive electrode. The results provide a unified understanding of energy level alignment at electrode/HCM/perovskite interfaces and offer guidelines for the rational selection and design of HCM materials.

1. Introduction

Perovskite solar cells (PSCs) have seen a surge in interest because they can be fabricated by a low-cost solution process[1,2] and achieve a power conversion efficiency (PCE) of 27.3%.[3] Inverted structure (p-i-n type) devices, which are composed of a hole-collecting layer stacked on top of a transparent conductive electrode,[4] have been under intense scrutiny because they have lower processing temperature,[5] lower parasitic absorption loss in the front contact,[6,7] and greater stability[8] than conventional normal structure (n-i-p type) devices. The hole-collecting layer is made of polymers, including poly(3,4-ethylenedioxythiophene)-poly(styrenesulfonate) (PEDOT:PSS)[9,10] and poly[bis(4-phenyl)(2,4,6-trimethylphenyl) amine] (PTAA).[11] However, because its thickness exceeds 10 nm,[12–14] light transmission and electrical conductivity are reduced.[15,16] A hole-collecting monolayer (HCM) has been proposed as an alternative to polymer-based hole-collecting layers. As HCM is very thin (approximately 1 nm)[15,17] and is firmly bound to the transparent conductive electrode, parasitic light absorption is negligible,[15,16,18] and high device stability is achieved.[19] Incorporating HCM into PSCs improves the PCE of single-junction PSCs to 26.9% (ref. 20) and that of crystal-Si/halide perovskite tandem solar cells to 33.7%.[21]

An HCM molecule typically consists of a backbone that collects holes from the perovskite layer, an anchoring group that binds to the substrate, and a linker that connects the backbone and the anchoring group. Initially, carbazole derivatives are used as the backbone.[19,22,23] Subsequently, various HCMs have been developed by changing the alkyl chain length, substituents, and molecular backbone.[19,22,23]

The performance of HCMs is dependent on several factors, including wettability,[15] film density and uniformity,[24] defect passivation capability at the perovskite interface,[25] orbital overlap with the perovskite surface,[26] and charge transport properties.[27] Energy level alignment is the most fundamental and critical factor for efficient hole collection and electron-blocking capability,[28,29] because hole collection cannot be achieved without proper energy level alignment, even if all other properties are satisfied. Nevertheless, no consensus has been reached regarding the electrode/HCM/perovskite interface,

---

[a] *Graduate School of Engineering, Chiba University, 1-33 Yayoi-cho, Inage-ku, Chiba, 263-8522, Japan. E-mail: hyoshida@chiba-u.jp*

[b] *Institute for Chemical Research, Kyoto University, Gokasho, Uji, Kyoto, 611-0011, Japan*

[c] *i-Powered Energy System Research Center (i-PERC), The University of Electro-Communications, 1-5-1 Chofugaoka, Chofu, Tokyo, 182-8585, Japan*

[d] *Molecular Chirality Research Center, Chiba University, 1-33 Yayoi-cho, Inage-ku, Chiba, 263-8522, Japan*

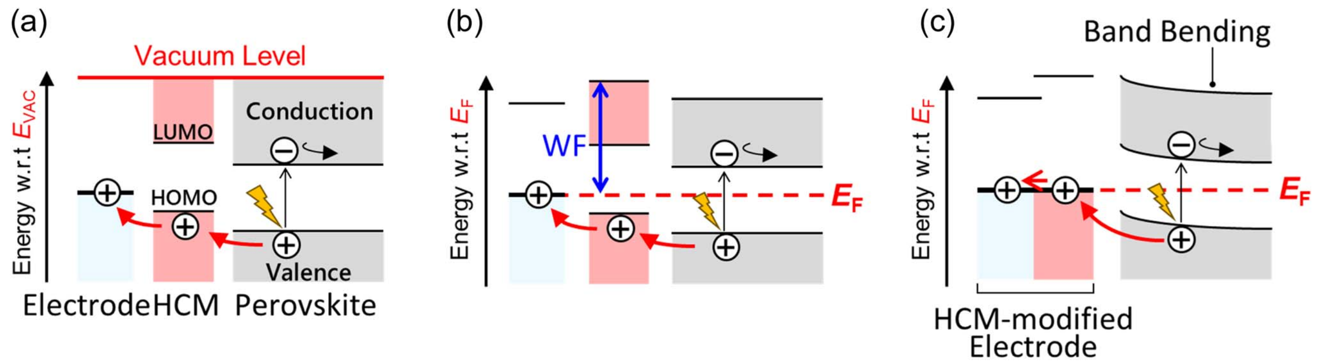

Fig. 1 Widely used models for energy level alignment at electrode/HCM/perovskite interfaces. (a) Vacuum level alignment model. (b) Fermi level alignment model. (c) Schottky model of HCM-modified electrode and perovskite. WF and E_F denote work function and Fermi level, respectively.

making the selection of an appropriate HCM or the design of new HCMs challenging.

To this end, it is essential to predict hole collection and electron-blocking efficiencies using a universal model for energy level alignment, which is based on fundamental energy parameters, such as ionization energy and work function. Three models for energy level alignment at electrode/HCM/perovskite interfaces are extensively used, as illustrated in Fig. 1a–c. The first one (Fig. 1a) is the vacuum level alignment model,[25,30,31] in which the vacuum levels of the three materials are assumed to align. This model is widely used because it requires only the ionization energies of individual materials, which are separately measured. However, this model ignores interface effects, such as interface dipole and band bending. The second model (Fig. 1b) assumes Fermi level alignment.[32–34] This model requires the work functions of the materials in addition to the ionization energies. The Fermi level alignment seems more reasonable than the vacuum level alignment because, according to the standard theory of solid-state physics, the energy levels should align with respect to the Fermi level when they come into contact. However, this model does not include band bending. In the third model shown in Fig. 1c, HCM is treated as a work function modifier for an electrode.[35–38] Energy level alignment between the perovskite and the HCM-modified electrode is predicted on the basis of the Schottky model for a metal/semiconductor contact. Hole collection efficiency is governed by band bending in the perovskite layer. For this model, the work function of the HCM-modified electrode and the work function/ionization energy of the perovskite layer are required. So far, these three models have been employed in various studies without a clear rationale.

In this study, we propose a model for energy level alignment at the electrode/HCM/perovskite interfaces, which successfully explains differences in photovoltaic performance. As model systems, we examine three representative carbazole-derived HCM materials—[2-(9*H*-carbazol-9-yl)ethyl]phosphonic acid (2PACz),[25] [2-(3,6-dimethoxy-9*H*-carbazol-9-yl)ethyl]phosphonic acid (MeO-2PACz),[25] and [[5*H*-diindolo[3,2-a:3′,2′-c]carbazole-5,10,15-triyl]tris(propane-3,1-diyl)]tris(phosphonic acid) (3PATAT-C3).[26] The energy parameters in the solid phase of these HCMs and a mixed-composition perovskite, $Cs_{0.05}FA_{0.80}MA_{0.15}PbI_{2.75}Br_{0.25}$ (ref. 39) (hereinafter abbreviated as MixA-PVK1), are precisely measured using ultraviolet photoelectron spectroscopy (UPS) and low-energy inverse photoelectron spectroscopy (LEIPS).[40] We analyze the interface energy level alignment model in relation to photovoltaic performance. We find that the HCM/perovskite interface is well described by a semiconductor heterojunction model that has been established for the p–n junction of inorganic semiconductors,[41] whereas the electrode/HCM interface is treated in terms of interface dipole formation.[42] This model is further tested with other combinations of perovskites and HCMs, confirming its universal applicability.

As perovskites, $Cs_{0.05}FA_{0.73}MA_{0.22}PbI_{2.31}Br_{0.69}$ (ref. 25) (FA and MA denote formamidinium and methylammonium, respectively; this perovskite is hereinafter abbreviated as MixA-PVK2), a mixed-composition perovskite; $MAPbI_3$, a representative lead-based perovskite; and $FASnI_3$, a tin-based perovskite that is attracting attention as a lead-free perovskite, are employed.

For the additional HCMs, we examine Me-PhpPACz,[43] Br-2EPT,[44] MeO-BTBT,[45] 4PADCB,[46] ID-Cz,[47] Py3,[48] MPA-BT-XA,[30] and 4-XPBA[49] (see Section S4.2 of SI for brief descriptions of each molecule). These HCMs are selected to cover broad structural and electronic diversity, enabling rigorous evaluation of the universality of the proposed model. The energy parameters are taken from the literature, and the predicted hole collection efficiency using the model is compared with experimentally measured photovoltaic performance, such as open circuit voltage V_{oc}, short circuit current J_{sc}, fill factor FF, and PCE. These tests demonstrate that our proposed model is generally applicable to electrode/HCM/perovskite interfaces.

In this model, the ionization energy and the work function of HCMs are critical energy parameters. Thus, we further clarify the factors governing them. Our findings provide practical guidelines for the selection and design of HCM molecules.

2. Models for energy level alignment at electrode/HCM/perovskite interfaces

2.1. Experimental determination of energy parameters

Fig. 2a and b show the results of UPS and LEIPS measurements of ITO as well as 2PACz, MeO-2PACz, and 3PATAT-C3 films

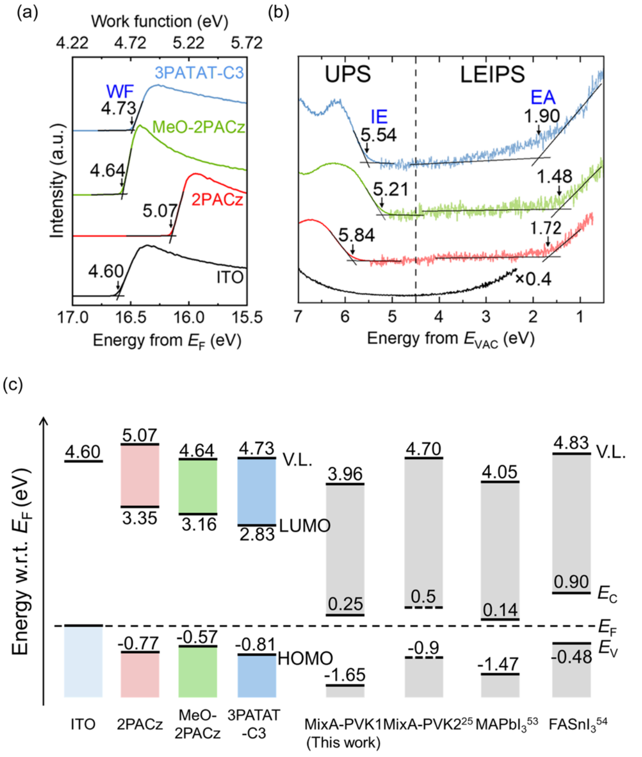

Fig. 2 (a) The secondary electron cut-off region of UPS showing the work functions of ITO and HCMs. (b) UPS and LEIPS spectra around the Fermi level (the energy with reference to the vacuum level), the onset of which corresponds to the ionization energy (IE) and the electron affinity (EA). (c) Energy parameters obtained by UPS and LEIPS are summarized with reference to the Fermi level. VB and CB edge values (literature values) for various perovskites are also shown. MixA-PVK1 and MixA-PVK2 denote $Cs_{0.05}FA_{0.80}MA_{0.15}PbI_{2.75}Br_{0.25}$ and $Cs_{0.05}FA_{0.73}MA_{0.22}PbI_{2.31}Br_{0.69}$, respectively. MixA-PVK1 corresponds to the perovskite measured experimentally. E_C, E_V, E_F, and V.L. refer to CB edge, VB edge, Fermi level, and vacuum level, respectively. Solid and dashed lines of the VB edge of the perovskites are determined from the logarithmic and linear scales of UPS spectra, respectively (see Fig. S1 in SI). For the CB edge of the perovskites, the values for MixA-PVK1, $MAPbI_3$, and $FASnI_3$ were determined from LEIPS, and that for MixA-PVK2 was determined from the optical bandgap.

prepared on an ITO substrate. The spectrum of pristine ITO is also shown for comparison. The work functions are derived from the secondary electron cut-off of UPS (Fig. 2a). The work function of pristine ITO is 4.60 eV. This is altered when HCMs are adsorbed onto ITO: it increases to 5.07 eV in 2PACz but remains almost unchanged in MeO-2PACz (4.64 eV) and 3PATAT-C3 (4.73 eV). The work function of perovskite MixA-PVK1 prepared on the ITO substrate is 3.96 eV, as shown in Fig. S1 of SI. Fig. 2b shows the UPS and LEIPS spectra. The HOMO levels determined from the UPS spectral onsets are similar among 2PACz (−0.77 eV), MeO-2PACz (−0.57 eV), and 3PATAT-C3 (−0.81 eV) with respect to the Fermi level. The LUMO levels determined from the LEIPS spectra are more than 2.5 eV above the Fermi level,[50] ensuring efficient electron-blocking capability. Because the Fermi levels are located close to the HOMO levels, 2PACz, MeO-2PACz, and 3PATAT-C3 are expected to behave as p-type semiconductors. The valence band (VB) edge and the conduction band (CB) edge, corresponding to the ionization energy and the electron affinity of perovskite MixA-PVK1, are determined from the UPS and LEIPS spectral onsets on a logarithmic scale[51,52] as 5.61 eV and 3.71 eV, respectively (Fig. S1). The bandgap is 1.9 eV, approximately 0.3 eV larger than the optical bandgap of 1.57 eV.[39] It has been pointed out that UPS/LEIPS may give a very weak signal for the band edge owing to the selection rule (momentum conservation) and that the band edge may be detected only when the spectra are plotted on a logarithmic scale.[51,52] In this study, we use the CB edge value obtained by LEIPS to evaluate the electron transport level, as electrons are introduced into CB during the LEIPS process. Unfortunately, UPS data on a logarithmic scale cannot be obtained for MixA-PVK2. Therefore, the VB edge derived from the linear-scale spectra is used instead. Fig. 2c shows the energy level diagram with respect to the Fermi level. The perovskite MixA-PVK1 energy levels demonstrate no noticeable dependence on the underlying HCM, as confirmed by measurements of films deposited on substrates having various work functions (see Section S1.2 of SI). Therefore, the energy levels measured for the perovskite film prepared on ITO are used hereinafter. Fig. 2c also presents the energy parameters of various perovskites taken from the literature,[25,53,54] which are used in the following discussion. The corresponding energy level diagram referenced to the vacuum level is provided in Fig. S3.

2.2. Assessment of conventional energy-level alignment models

Based on the energy parameters obtained above, we discuss the validity of the three models shown in Fig. 1, in comparison with the photovoltaic performance for each HCM used with MixA-PVK1. Other typical perovskites, including MixA-PVK2, $MAPbI_3$,[53] and $FASnI_3$,[54] are discussed in the SI (see Section S2 of SI). The device configuration is ITO/HCM/MixA-PVK1/C_{60}/BCP/Ag.[26] Fig. 3 and Table 1 show the *J*–*V* curves and performance parameters of PSCs. These results clearly show the inferior photovoltaic performance of 2PACz compared to MeO-

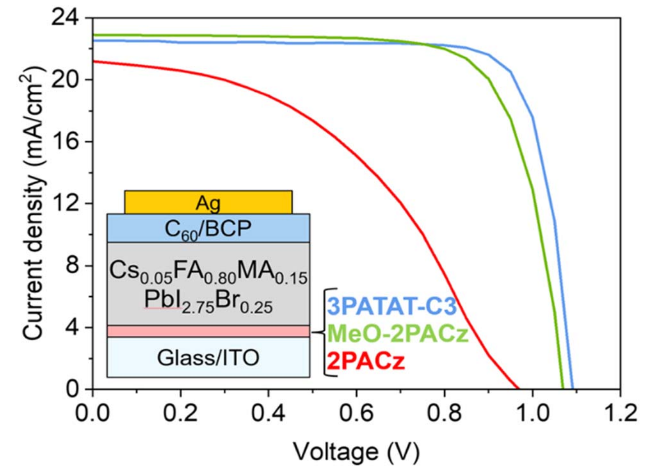

Fig. 3 *J*–*V* curves of PSC, ITO/HCM/MixA-PVK1/C_{60}/BCP/Ag, where HCM is 2PACz (red curve), MeO-2PACz (green curve), or 3PATAT-C3 (blue curve).

Table 1 Photovoltaic performance with different HCMs

HCM	Scan[a]	J_{sc} [mA cm^{-2}]	V_{oc} [V]	FF [%]	PCE [%]
2PACz	F	21.2	0.97	44.1	9.1
	R	21.0	1.02	54.1	11.6
MeO-2PACz	F	22.9	1.07	74.2	18.2
	R	22.9	1.06	77.9	18.9
3PATAT-C3	F	22.5	1.09	79.3	19.5
	R	22.4	1.10	81.6	20.1

[a] Forward (F) and reverse (R) indicates the scan direction from J_{SC} to V_{OC} and from V_{OC} to J_{SC}, respectively.

2PACz and 3PATAT-C3. We evaluate the above three models to determine whether they adequately explain the difference in photovoltaic performance.

First, we discuss the vacuum level alignment model shown in Fig. 1a. The corresponding energy level diagram is given in Fig. S3. The LUMO levels of all HCMs are more than 1 eV above the CB edge of MixA-PVK1, indicating good electron-blocking capability. Regarding the hole collection efficiency, the HOMO levels of MeO-2PACz and 3PATAT-C3 are 0.40 and 0.07 eV higher than the VB edge of MixA-PVK1. In contrast, the HOMO level of 2PACz is 0.23 eV lower than the VB edge, suggesting low hole collection efficiency only for 2PACz. This model explains the inferior photovoltaic performance of 2PACz. However, this model contradicts the observation of the secondary electron cut-off (Fig. 2a) that the vacuum level is not constant but shifts by as much as 0.47 eV when HCM is adsorbed on the electrode. The origin of the vacuum level shift will be discussed later.

Second, we discuss the Fermi level alignment model shown in Fig. 1b. The energy level diagram (Fig. 2c) indicates that the LUMO levels of all the HCMs are more than 2.5 eV above the CB edge of MixA-PVK1. The HOMO levels of all the HCMs are positioned 0.84–1.08 eV above the VB edge of MixA-PVK1. Although 2PACz shows there is a large vacuum level shift of 0.47 eV, the HOMO and LUMO levels are similar among the HCMs. Therefore, we predict similar hole collection efficiency and electron-blocking capability for these HCMs, which do not explain the observed photovoltaic performance.

Third, we discuss the Schottky model shown in Fig. 1c. Fig. S4 shows the energy level alignments with respect to various perovskites. A considerable upward band bending of 0.68–1.11 eV for MixA-PVK1 is predicted for the three HCMs, which is favorable for hole collection and electron blocking. Therefore, the inferior performance of 2PACz cannot be explained by this model.

As we have seen earlier, the first vacuum-alignment model (Fig. 1a) can explain the variation in photovoltaic performance. However, it contradicts the experimental observation of vacuum level variation (Fig. 2a). On the other hand, the second Fermi-alignment model (Fig. 1b) and third (Schottky (Fig. 1c) model cannot explain the inferior performance of the solar cell that uses 2PACz as the HCM. Therefore, we need to develop an alternative model that can adequately explain the photovoltaic performance and at the same time has a sound physical basis.

2.3. Development of a unified energy-level alignment model

The outline of our newly developed model of electrode/HCM/perovskite interfaces is shown in Fig. 4a. The interfaces around HCMs can be treated by separating them into the electrode/HCM interface and the HCM/perovskite interface. For the electrode/HCM interface, we consider only the interface dipole, which has been discussed extensively for the metal/organic semiconductor interface.[42] Band bending of the HCM layer is ignored because this layer is too thin (on the order of 1 nm) to hold a sufficient magnitude of the band bending.[55] The magnitude and the origin of the interface dipole will be discussed later in the framework of the dipole layer at the metal/organic interface.[42] In contrast to the electrode/HCM interface, there are no established models for the HCM/perovskite interface. We apply the semiconductor heterojunction theory,[41] treating both HCM and perovskite layers as semiconductors with different band gaps. This means that hole conduction occurs through the HOMO level of the HCM and the VB edge of the perovskite. This is different from the previously discussed model based on the Schottky model (Fig. 1c) in which the HCM is treated as a work function modifier of the electrode. It has

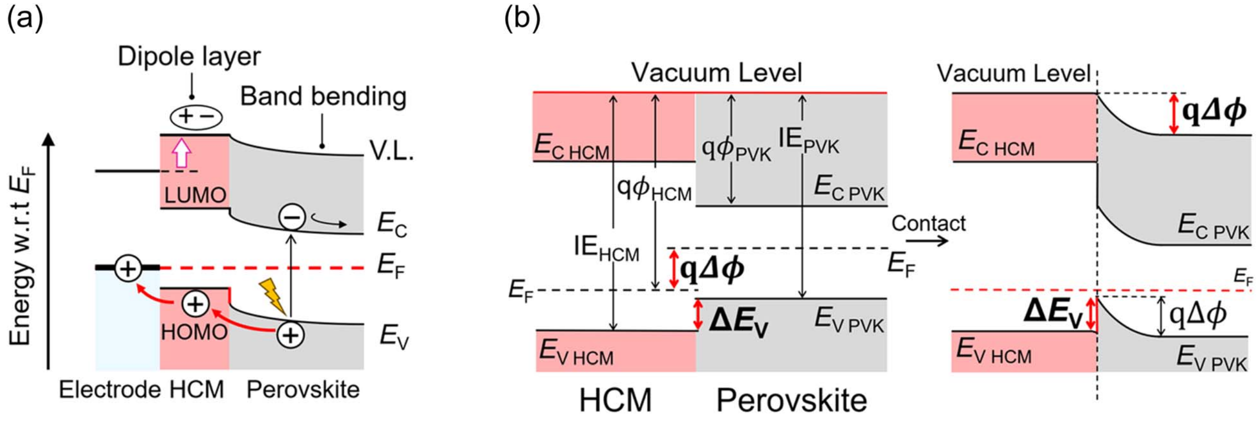

Fig. 4 (a) Energy level alignment at electrode/HCM/perovskite interfaces proposed in this work. (b) Energy levels and band bending focusing on the HCM/perovskite interface, which is treated as a semiconductor heterojunction. The left side illustrates the energy levels prior to contact, which align to the vacuum level. The right side illustrates those after contact, wherein the energy levels align at the Fermi level.

been reported that the density of deep defect levels on the perovskite surface is extremely low (below 10 ppm). Therefore, the Fermi level of the perovskite layer is not pinned when it reaches thermal equilibrium with the substrate. As a result, the Fermi level can shift across the entire bandgap.[56] Therefore, it is reasonable to consider band bending on the perovskite side in this model as well.

Fig. 4b illustrates a procedure for constructing an energy level diagram with band bending at the HCM/perovskite heterojunction. Prior to contact, the energy levels align to the vacuum level. Upon contact, the Fermi levels of the two layers equilibrate. This interaction causes the vacuum levels to bend continuously from the HCM to the perovskite, while maintaining the ionization energy and the electron affinity.

The hole collection efficiency is influenced by the band bending direction and the barrier height at the interface (Fig. 4b), as summarized below:

(1) The band bending direction is determined by the work function difference ($\Delta\Phi$) between the HCM (Φ_{HCM}) and the perovskite (Φ_{PVK}). When $\Phi_{\mathrm{HCM}} > \Phi_{\mathrm{PVK}}$ (positive $\Delta\Phi$), VB and CB of the perovskite bend upwards towards the interface, which is favorable for hole collection and electron blocking. When $\Phi_{\mathrm{HCM}} = \Phi_{\mathrm{PVK}}$, no band bending occurs. Conversely, when $\Phi_{\mathrm{HCM}} < \Phi_{\mathrm{PVK}}$, VB and CB bend downwards towards the interface, which is not preferable for hole collection.

(2) The barrier height at the interface for holes (ΔE_{V}) is determined by the difference in ionization energy between the HCM ($\mathrm{IE}_{\mathrm{HCM}}$) and the perovskite ($\mathrm{IE}_{\mathrm{PVK}}$). A negative barrier height $\Delta E_{\mathrm{V}} = \mathrm{IE}_{\mathrm{HCM}} - \mathrm{IE}_{\mathrm{PVK}}$ is favorable for hole collection. On the other hand, the barrier height for electrons (ΔE_{C}) is influenced by the difference in electron affinity between the HCM ($\mathrm{EA}_{\mathrm{HCM}}$) and the perovskite ($\mathrm{EA}_{\mathrm{PVK}}$). A large negative value of $\mathrm{EA}_{\mathrm{HCM}} - \mathrm{EA}_{\mathrm{PVK}}$ is favorable for efficient electron blocking.

2.4. Model validation using representative HCMs

We apply our heterojunction model to MixA-PVK1, whose photovoltaic performance has been discussed above (Fig. 3). As shown in Fig. 5a, the upward band bending $\Delta\Phi$ of 0.68–1.11 eV occurs in the perovskite layer toward the interface for all HCMs. An energy barrier ΔE_{V} of 0.23 eV is predicted for 2PACz, whereas no ΔE_{V} is predicted for MeO-2PACz and 3PATAT-C3. As a result, MeO-2PACz and 3PATAT-C3 can efficiently collect holes, but 2PACz cannot. This prediction is consistent with the low photovoltaic performance observed in 2PACz. This is a good example of hole collection efficiency being governed by ΔE_{V}. Because the energy barrier ΔE_{V} is determined by the ionization energy, the vacuum level alignment model (Fig. 1a) is able to explain the photovoltaic performance by chance.

We apply the present model to other perovskites, including MixA-PVK2, $\mathrm{MAPbI_3}$,[53] and $\mathrm{FASnI_3}$.[54] In MixA-PVK2, the band bending $\Delta\Phi$ plays a main role. Fig. 5b shows the energy level alignment between the HCMs (2PACz and MeO-2PACz) and MixA-PVK2. Their energy parameters are obtained from the literature.[25] The energy barriers ΔE_{V} of 2PACz and MeO-2PACz are 0 eV and −0.5 eV, respectively. Thus, no ΔE_{V} for hole collection is formed at the interface. However, $\Delta\Phi$ differs between them; it is 0.3 eV for 2PACz and −0.1 eV for MeO-2PACz. Therefore, our model predicts that 2PACz exhibits higher hole collection efficiency than MeO-2PACz. Al-Ashouri and coworkers showed that the hole collection efficiency of 2PACz is more than two orders of magnitude higher than that of MeO-2PACz,[27] consistent with the prediction by our model.

We also discuss $\mathrm{MAPbI_3}$, a prototypical lead perovskite. This perovskite is characterized by a small work function Φ_{PVK} of 4.05 eV and a small ionization energy $\mathrm{IE}_{\mathrm{PVK}}$ of 5.52 eV.[53] As a result of the low Φ_{PVK}, an upward band bending $\Delta\Phi$ is predicted for all combinations of HCMs, which makes band bending for hole collection preferable, as shown in Fig. S5a. However, the energy barrier ΔE_{V} affects photovoltaic performance. We cannot find any reports on the photovoltaic performance of 2PACz and $\mathrm{MAPbI_3}$, likely because of their poor performance. 3PATAT-C3 forms an energy barrier ΔE_{V} of 0.02 eV, comparable to the thermal energy at room temperature (approximately 0.026 eV). Unfortunately, solar cell data are not available for 3PATAT-C3, probably because it is a new HCM. Nevertheless, we predict good performance because of the upward band bending $\Delta\Phi$ and the negligible energy barrier ΔE_{V}.

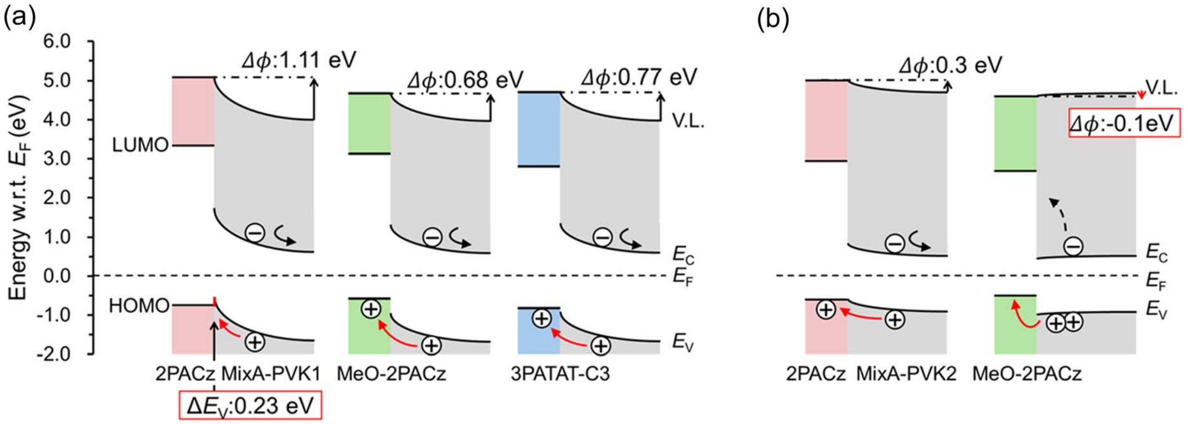

Fig. 5 Energy level diagrams at HCM/perovskite interfaces. The perovskites are (a) $\mathrm{Cs_{0.05}FA_{0.80}MA_{0.15}PbI_{2.75}Br_{0.25}}$ (MixA PVK1) and (b) $\mathrm{Cs_{0.05}FA_{0.73}MA_{0.22}PbI_{2.31}Br_{0.69}}$ (MixA PVK2).

Conversely, MeO-2PACz forms no energy barrier ΔE_V at the interface, consistent with a report on a high PCE of 19.8% for inverted PSCs using MeO-2PACz.[25]

The next example is a promising candidate for lead-free perovskite, $FASnI_3$. This tin perovskite is characterized by a large work function Φ_{PVK} of 4.83 eV and a small ionization energy IE_{PVK} of 5.31 eV, showing p-type semiconductor behavior.[54] Fig. S5b shows the energy level alignments between $FASnI_3$ and HCMs, 2PACz and MeO-2PACz, together with conventional hole-collecting layers, such as PEDOT:PSS and NiO_X. Table S1 summarizes photovoltaic performances from the literature together with band bending $\Delta\Phi$ and barrier height ΔE_V. In general, a large work function Φ_{PVK} and a small ionization energy IE_{PVK} for $FASnI_3$ lead to downward band bending $\Delta\Phi$ and/or positive energy barrier ΔE_V, resulting in low hole collection efficiency. This prediction is consistent with the finding that HCMs are not effective for $FASnI_3$ PSCs.[57] It is essential to develop HCMs with a small ionization energy IE_{HCM}. As we will discuss later, the ionization energy IE_{HCM} is determined by the ionization energy of the isolated molecule, indicating that the carbazole-based HCMs may not be suitable for the tin perovskite. The present carbazole-based HCMs can be used if the work function Φ_{PVK} of the tin perovskite is decreased by n-doping. This issue may be resolved by the low coverage of the 4-XPBA (X = N, C, TF, and F), as discussed below.[49] On the other hand, the model predicts good photovoltaic performance for $FASnI_3$ with PEDOT:PSS, consistent with the excellent V_{oc}, J_{sc}, and FF values (Table S1). Furthermore, a high PCE of 14.81% has been achieved in the system modified with a 2D perovskite.[58] In the case of NiO_x, the energy barrier ΔE_V is predicted, similar to that of 2PACz. A comparison of photovoltaic parameters indicates that both hole collecting materials show inferior PCE.[59] Further quantitative investigation is needed to clarify how the band bending $\Delta\Phi$ and the energy barrier ΔE_V influence V_{oc}, J_{sc}, and FF.

Through these results, we have demonstrated that our heterojunction model can predict the photovoltaic performance of four perovskites, which are characterized by different combinations of work functions Φ and ionization energies IE, namely, MixA-PVK1 (small Φ and large IE), MixA-PVK2 (large Φ and large IE), $MAPbI_3$ (small Φ and small IE), and $FASnI_3$ (large Φ and small IE).

2.5. General applicability of the model to diverse HCM and perovskite systems

Next, we extend our model beyond the carbazole-based systems discussed above. We survey literature comparing two or more HCMs in terms of energy levels and photovoltaic performance. In one example, the improved performance of a newly developed HCM is demonstrated compared with conventional HCMs, such as 2PACz and MeO-2PACz. In other examples, a series of HCMs with different substituents are compared to elucidate substituent effects. Using data from those studies, we examine the correlation between photovoltaic performance and hole collection efficiency predicted by our model.

We investigate the following representative compounds: Me-PhpPACz, in which a benzene ring is introduced into the linker to enhance conductivity and photostability;[43] Br-2EPT, which employs a phenothiazine backbone as a cost-effective alternative to the carbazole backbone;[44] MeO-BTBT, which is based on the BTBT backbone known for its air stability and superior hole-transporting properties;[45] 4PADCB, which extends the π-conjugated carbazole system and introduces steric hindrance to suppress molecular aggregation;[46] IDCz, which incorporates two anchoring groups to control molecular orientation and form a dense film;[47] Py3, which utilizes a pyrene core to achieve dense film formation through π–π interactions;[48] MPA-BT-XA (X = C, B, and R), which employs a donor–acceptor-type backbone and carboxylic acid anchoring groups;[30] and 4-XPBA (X = N, C, TF, and F), a small molecule using phenylboronic acid as the anchoring group.[49] For MeO-BTBT and MPA-BT-XA, the perovskite energy levels were not reported in the same paper; therefore, we adopt literature values for a perovskite with the same composition.[60,61]

First, the relevant energy parameters are taken from the literature, and their validity is carefully assessed. The determination of the perovskite valence band (VB) edge varies across studies, depending on whether it is derived from a logarithmic or a linear intensity scale, hereinafter referred to as $E_{V\text{-}Log}$ or $E_{V\text{-}Linear}$, respectively. Based on the comparison between $E_{V\text{-}Log}$ and $E_{V\text{-}Linear}$ (see Section S4.1 of SI), we assume that $E_{V\text{-}Log}$ is 0.3 eV above $E_{V\text{-}Linear}$ for references reporting only $E_{V\text{-}Linear}$. Using these values, we calculate energy barrier heights $\Delta E_{V\text{-}Linear}$ and $\Delta E_{V\text{-}Log}$ by subtracting the $E_{V\text{-}Linear}/E_{V\text{-}Log}$ of perovskite from the ionization energy of HCMs.

Using these ionization energies and work functions, we predict from the energy barriers ΔE_V and the magnitude of band bending $\Delta\Phi$ whether the energy level alignment is favorable for hole collection based on the model. The detailed analysis and the energy level diagrams are provided in Section S4.2 of SI. These predictions are then compared with reported photovoltaic performance metrics, such as J_{sc}, V_{oc}, FF, and PCE. Table 2 summarizes the photovoltaic performance and the predicted hole collection efficiencies. Analysis of a wide range of HCMs demonstrates that photovoltaic performance is consistently governed by the interfacial energy barrier ΔE_V and the band bending $\Delta\Phi$. HCMs exhibiting negligible energy barriers and favorable upward band bending show superior hole collection efficiency and high photovoltaic performance, whereas downward band bending or interfacial barrier reduces PCE. In most cases, the proposed model successfully explains the observed performance trends across diverse molecular backbones.

The only exception is the 4-XPBA (X = N, C, TF, and F) series. The trend of PCE follows the magnitude of upward band bending $\Delta\Phi$; however, these HCMs form a large energy barrier, ΔE_V, exceeding 1 eV. It appears that these HCMs function as a work function modifier, consistent with the earlier model shown in Fig. 1c. However, the earlier model cannot account for the inferior performance of MeO-2PACz. We found that the coverage of 4-XPBA is only one-quarter of that of MeO-2PACz, suggesting that holes are collected directly at the FTO electrode rather than transported through the HCM. This results in 4-XPBA acting as a work function modifier because of the low coverage. In contrast, MeO-2PACz fully covers the electrode, resulting in an energy barrier of 0.18 eV and reduced hole

Table 2 Summary of photovoltaic performance and energy parameters

		Photovoltaic performance				Energy parameter and predicted hole collection efficiency		
Ref.	HCM	J_{SC} [mA cm^{-2}]	V_{OC} [V]	FF [%]	PCE [%]	Band bending$\Delta\Phi^{a}$ [eV]	Barrier heightΔE_{V}^{a} [eV]	Predicted efficiency^{b}
π-Conjugated linker								
43	Me-4PACz	25.23	1.177	81.30	24.14	0.43	−0.31	△
	Me-PhpPACz	25.37	1.189	86.79	26.17	0.53	−0.22	○
Phenothiazine backbone								
44	MeO-2PACz	24.96	1.06	80	21.16	−0.58	−0.34	×
	Br-2EPT	25.11	1.09	82	22.44	0.02	−0.21	○
BTBT backbone								
45	MeO-2PACz	24.62	1.134	83.45	23.29	0.10	−0.31	△
	MeO-BTBT	24.82	1.159	85.28	24.53	0.21	−0.16	○
π-Extended backbone								
46	4PACz	17.80	1.26	75.49	16.93	−0.03	0.27	×
	4PADCB	17.84	1.30	78.70	18.28	−0.13	−0.09	△
Dual anchoring groups								
47	IDCz-1	25.27	1.01	81.92	20.97	−0.07	−0.75	△
	IDCz-2	25.43	1.11	81.61	23.11	0.02	−0.63	△
	IDCz-3	25.59	1.16	84.74	25.15	0.27	−0.46	○
Pyrene backbone								
48	2PACz	25.3	1.14	80.0	23.1	−0.12	−0.07	△^{c}
	Py3	26.0	1.18	85.1	26.1	−0.35	−0.40	△^{c}
Donor–acceptor backbone								
Carboxylic acid anchor								
30	MPA-BT-RA	22.03	1.10	81.1	19.65	0.06	−0.24	△
	MPA-BT-BA	22.76	1.12	81.0	20.58	0.60	−0.29	△
	MPA-BT-CA	23.18	1.15	82.0	21.81	0.73	−0.19	○
Phenylboronic acid anchor								
49	MeO-2PACz	25.85	0.45	45.3	9.27	0.38	0.18	×
	4-FPBA	26.97	0.81	65.1	14.21	0.08	1.34	△
	4-TFPBA	27.42	0.83	68.7	15.69	0.12	1.35	△
	4-CPBA	27.66	0.84	73.0	17.00	0.28	1.47	△
	4-NPBA	27.89	0.86	76.3	18.37	0.33	1.46	○

[a] A positive value means upward band bending and the energy barrier for holes. [b] Predicted hole collection efficiency from band bending and energy barrier. ○, △, and × denote high, moderate, and low hole collection efficiency. [c] This prediction changes when energy barrier ΔE_{V} is calculated using $\Delta E_{V\text{-}Log}$ (see Section S4.2 of SI).

collection efficiency (Fig. S7h). This suggests that the low hole collection efficiency of MeO-2PACz is explained by an interfacial energy barrier ΔE_{V} that is not included in the previous model. The hole collection efficiency independent of the barrier height can also be explained by the tunneling through the HCM layer owing to its short molecular length compared with MeO-2PACz. The details are discussed in ref. 49. Overall, these results confirm the broad applicability of the proposed energy level alignment model across diverse HCM and perovskite systems.

From these results, we conclude that HCMs exhibiting high photovoltaic performance always possess no or negligible energy barrier ΔE_{V} and favorable upward band bending $\Delta \Phi$ of the perovskite. We emphasize that these are the necessary conditions to achieve efficient hole collection. As highlighted in recent reviews,[19,22,23] many other factors also influence HCM performance, including wettability, film density and uniformity, defect passivation at the perovskite interface, orbital overlap with the perovskite surface, charge transport properties, grain size, and defect density.[43,45] However, achieving high hole collection efficiency always requires favorable energy level alignment as a necessary condition, which must be satisfied prior to the other factors.

3. Factors determining HCM ionization energy and work function

To construct the energy level diagram at the electrode/HCM/perovskite interfaces, we require the work functions and the ionization energies of the perovskite and HCM, as well as the work function of the electrode. To understand the factors that govern the work function and the ionization energy of HCMs, we measure 3PATAT-C3 films prepared on electrodes with different work functions, ITO_1, ITO_2, and FTO. Fig. 6a shows the UPS spectra from which we determine the work function and the ionization energy. The results are summarized in the energy level diagram depicted in Fig. 6b. The variation in the ionization energies of 3PATAT-C3 among the samples is within 0.2 eV. Conversely, the work function exhibits a significant difference, ranging from 4.1 to 4.7 eV. Interestingly, the work function is shifted similarly to that of the respective electrodes (dotted lines in Fig. 6a), meaning that the magnitude of the interface dipole generated by 3PATAT-C3, which is the difference in work function between the electrodes and the HCM, is nearly constant, with only a 0.1–0.2 eV variation. The result demonstrates that the work function of HCM is determined by

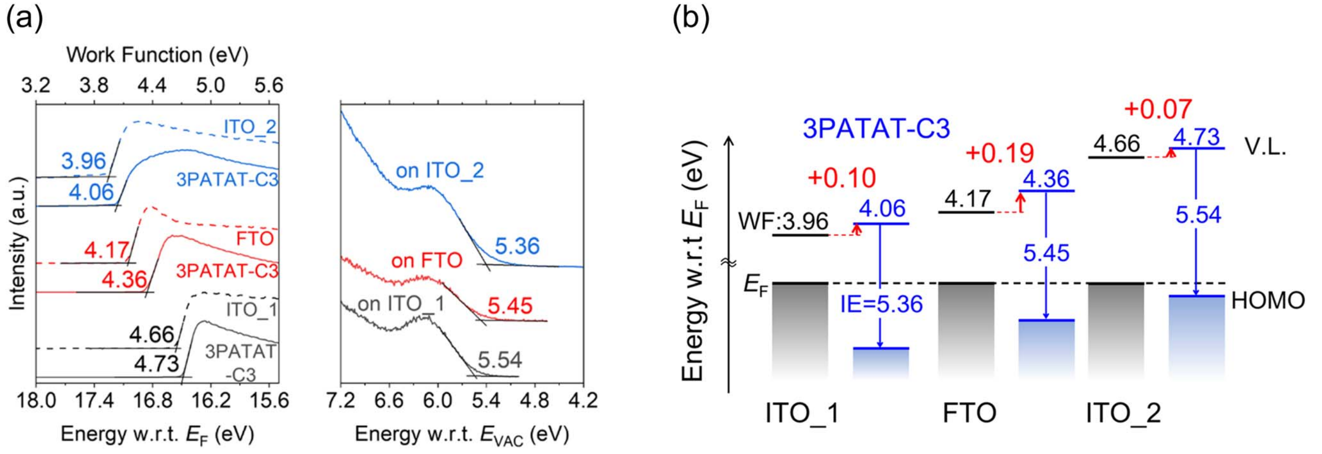

Fig. 6 Energy levels of 3PATAT-C3 prepared on electrodes with different work functions. (a) UPS spectra of the secondary electron cut-off region (left) and around the Fermi level (right). Solid and dashed lines indicate the spectra of 3PATAT-C3 and the transparent electrode, respectively. (b) Energy level diagram at the electrode/3PATAT-C3 interface.

that of the electrode, and HCM constantly shifts the electrode's work function through the formation of an interfacial dipole layer.

3.1. Magnitude of interface dipole generated by HCM

We further examine the interfacial dipole layer (work function shift) formed by the HCM, $\Delta\phi_{\mathrm{HCM}}$. At the metal/organic interface, various factors, including the push-back effect, interfacial charge transfer, chemical interaction, and the permanent dipole moment of an organic molecule, give rise to the interfacial dipole layer.[42] Here, we first consider the dipole layer $\Delta\phi_{\mathrm{HCM}}$ generated by the permanent dipole moment of the HCM molecule μ because the influence of other factors on the interfacial dipole may be small.[62] Considering the angle of the molecular dipole with respect to the surface normal θ and the molecular density N/A, $\Delta\phi_{\mathrm{HCM}}$ can be expressed using the Helmholtz equation,[63]

$$\Delta\phi_{\mathrm{HCM}} = \frac{e\mu_{\perp}}{\varepsilon_0\varepsilon_{\mathrm{eff}}}\frac{N}{A} = \frac{e\mu\cos\theta}{\varepsilon_0\varepsilon_{\mathrm{eff}}}\frac{N}{A} \tag{1}$$

where e is the elementary charge, ε_0 is the permittivity of the vacuum, and $\varepsilon_{\mathrm{eff}}$ is the effective permittivity. To discuss the interfacial dipole layer, we experimentally examine the molecular orientations of HCM on ITO and calculate the dipole moment of an isolated HCM molecule.

Determining the molecular orientation of HCM on a transparent conductive electrode (ITO or FTO) is not straightforward because standard techniques for analyzing molecular orientation, such as variable angle spectroscopic ellipsometry (VASE), multiple-angle infrared incidence resolution spectroscopy (MAIRS), near edge X-ray absorption fine structure (NEXAFS),[63,64] sum frequency generation (SFG),[62] and scanning probe microscopy, do not provide reliable results owing to surface roughness. In our previous work, we demonstrated that the combination of UPS and metastable atom electron spectroscopy (MAES) is a powerful technique and used it to determine that 3PATAT-C3 adopts a parallel orientation on ITO.[26] Although both UPS and MAES measure the density of states (DOS) of VB, they differ in probing depth. UPS uses ultraviolet photons as an excitation source, and the probing depth is a few nanometers owing to the mean free path of electrons.[65] On the other hand, MAES employs metastable atoms that excite only the outermost orbitals.[66] Fig. S8 illustrates a schematic of the UPS and MAES spectra for the determination of molecular orientation. The spectral intensities originating from σ and π orbitals are compared. In the UPS spectra, peaks from both orbital types are observed. In the MAES spectra, the π orbital peak is prominent when the molecules assume a parallel orientation. In contrast, the σ orbital peak is enhanced when the molecules assume a perpendicular orientation. Thus, the molecular orientation can be determined by comparing the peak intensities in the UPS and MAES spectra.[67–69]

Fig. 7a and b show the UPS and MAES spectra of 2PACz and MeO-2PACz. For 2PACz, the peaks from 0.0 eV to 7.0 eV and around 11.0 eV are more pronounced in the MAES spectrum. For MeO-2PACz, the features around 6.0 eV and 8.0 eV are more intense in the UPS spectrum, whereas the peaks near 10.0 eV show greater intensity in the MAES spectrum. To assign the observed peaks, we calculate the molecular orbital energies for single molecules of 2PACz and MeO-2PACz using the density functional theory (DFT) with the B3LYP functional and the basis set of 6-31G(d). The lower panels of Fig. 7a and b display the simulated spectra generated by convoluting the molecular orbital energy calculated for the isolated molecule with Gaussian functions (FWHM of 1.29 eV). The simulated spectrum corresponding to the total DOS excellently reproduces the experimental UPS spectrum. Then, we classify the molecular orbitals of 2PACz into three types, as shown in Fig. S9a: the π orbitals of the carbazole backbone (denoted as π orbitals), the σ orbitals of the carbazole backbone (σ orbitals), and those of the anchor group (anchor). For MeO-2PACz, we also consider the orbitals localized on the methoxy group (methoxy) in addition to the three orbital types (Fig. S9b). We simulate spectra corresponding to the partial DOS of the separate groups of orbitals.

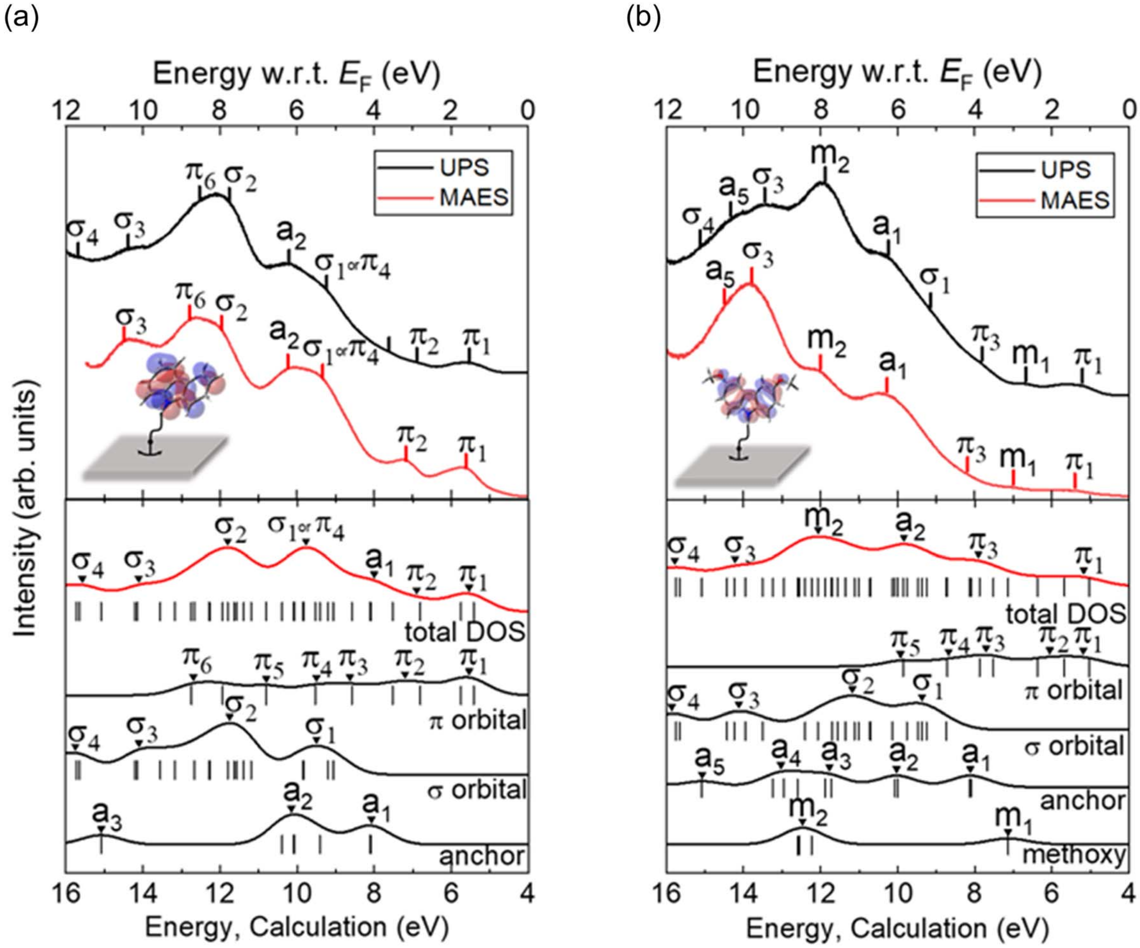

Fig. 7 Experimental UPS and MAES spectra (upper panels) and simulated total and partial DOSs (lower panels) of (a) 2PACz and (b) MeO-2PACz. In the simulation, the energies of the calculated molecular orbitals are indicated by vertical bars (black), whereas the simulated spectra (DOSs) are shown by solid lines (total DOS spectra are shown in red and partial DOS spectra in black).

We name the peaks in increasing order of binding energy, as follows: π_1, π_2,… for π orbitals; σ_1, σ_2,… for σ orbitals; a_1, a_2,… for the anchor group; and m_1 and m_2 for the methoxy group. We cannot distinguish between σ_1 and π_4 peaks owing to their proximity in energy. Thus, we refer to this peak as "σ_1 or π_4" in the total DOS spectrum shown in Fig. 7a. For 2PACz, the peaks at π_1, π_2, σ_1 or π_4, a_2, π_6, and σ_3 are more intense in the MAES spectrum than in the UPS spectrum. This suggests that both π and σ orbital peaks in the MAES spectrum are more pronounced, indicating that 2PACz is tilted with respect to the ITO normal, as illustrated in Fig. 7a. For MeO-2PACz, the peaks at σ_3 are much stronger in the MAES spectrum than the UPS spectrum. The predominance of σ orbital peaks suggests that the carbazole backbone is perpendicular to the ITO, as schematically shown in Fig. 7b. Some peak positions in the UPS and MAES spectra differ by 0.1 to 0.2 eV. These shifts may be due to variations in the electronic state between the outermost surface and the bulk of the sample,[70] or to the kinetic energy of the emitted electron being influenced by the interaction potential between the probe and the target surface.[66]

After analyzing the molecular orientations, we consider the permanent dipole moment μ appearing in eqn (1). The permanent dipole moment of each molecule is calculated using the DFT method with the B3LYP functional and the 6-31G(d) basis set on the Gaussian 16 program. The magnitudes of the dipole moment perpendicular to the surface are 1.57 D for 2PACz, 0.77 D for 3PATAT-C3, and −0.53 D for MeO-2PACz, as shown in Fig. 8a–c, respectively. Considering the dipole moment perpendicular to the surface and the tilted orientation of 2PACz, the substantial work function shift of 2PACz with respect to ITO is understandable. In contrast, the facts that the triazatruxene backbone of 3PATAT-C3 is parallel to ITO[26] and the molecular density N/A is small result in a small interface dipole and a reduced work function shift. MeO-2PACz exhibits a small dipole moment of −0.53 D perpendicular to the surface, leading to a minimal work function shift. It is noteworthy that the dipole moment of MeO-2PACz is influenced by the conformations of the two methoxy groups. As shown in Fig. 8c, the calculated perpendicular dipole moment is comparable to the previously reported value of approximately 0.3 D for MeO-Cz (the backbone of MeO-2PACz).[27] However, when the methoxy

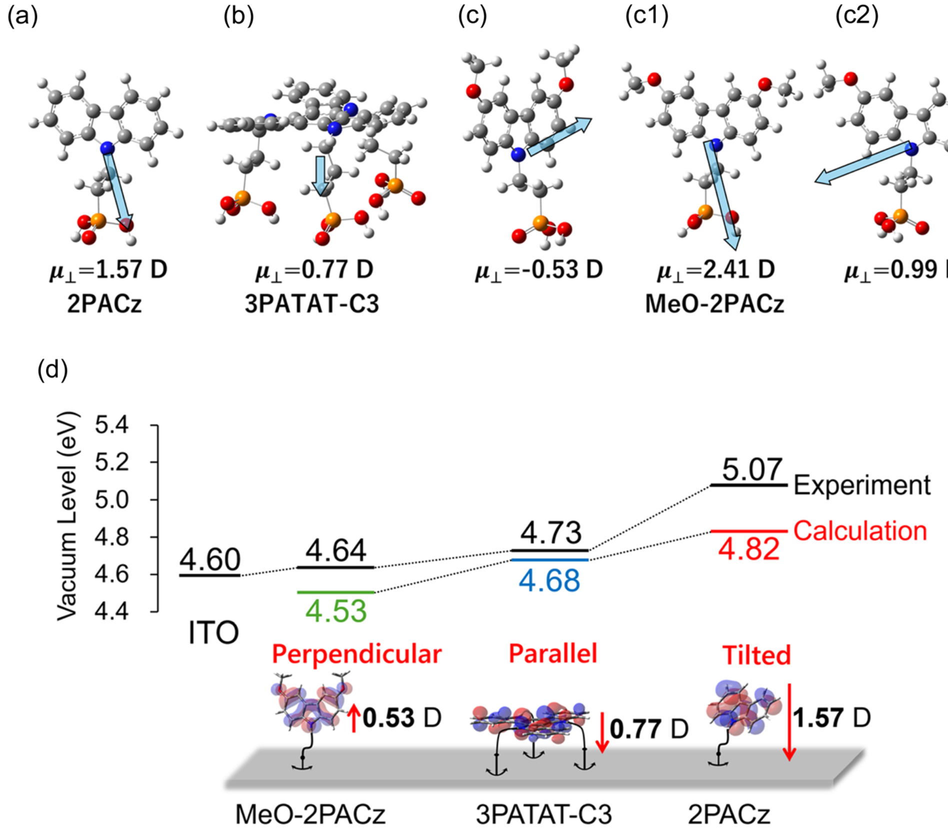

Fig. 8 Dipole layer of HCMs. The dipole moment of an isolated molecule is calculated using B3LYP/6-31G(d) for (a) 2PACz and (b) 3PATAT-C3. (c) (c1), and (c2) show MeO-2PACz with different conformations of the methoxy groups. Blue arrows indicate the magnitude and direction of the dipole moment. $\mu_\perp$ indicates the magnitude of the dipole moment normal to the substrate surface. (d) Calculated work functions utilizing the Helmholtz equation (eqn (1)) are compared with experimentally derived ones (Fig. 2a).

groups rotate to assume a downward conformation, as depicted in Fig. 8c1 and c2, the perpendicular dipole moment drastically increases to 2.41 D and 0.99 D. From our observations of molecular orientation and the small work function shifts, we conclude that the methoxy group of MeO-2PACz adopts an upward conformation, as shown in Fig. 8c. This is confirmed by the total energies of the three conformations calculated by DFT. The conformer shown in Fig. 8c is the most stable, and the conformers shown in Fig. 8c1 and c2 have 49 meV and 23 meV higher energies, respectively, than that shown in Fig. 8c. These results also indicate that the most stable conformation of the methoxy groups is upward, which contributes to the small perpendicular dipole moment and the small work function shift.

On the basis of the molecular orientation, the molecular dipole moments, and the molecular density, we calculate the magnitude of the dipole layer (the work function) using eqn (1). The molecular density *N*/*A* is taken from the literature;[26] it is 1.04×10^{13} cm^{-2} for 3PATAT-C3 and 7.12×10^{13} cm^{-2} for MeO-2PACz. For 2PACz, we assume the same value as that for MeO-2PACz. We set $\varepsilon_{\text{eff}} = 1.9$ as it is reported that ε_{eff} falls in the range of 1.9 to 2.0.[71] The calculated work functions of 2PACz, 3PATAT-C3, and MeO-2PACz are 4.82 eV, 4.68 eV, and 4.53 eV, respectively, which align closely with the experimental values shown in Fig. 8d. This agreement between the calculated and experimental values confirms that the magnitude of the dipole layer formed by the HCM layer is determined by the molecular orientation, the dipole moment of the isolated molecules, and the molecular density. It is noteworthy that the vacuum level shift predicted from the permanent dipole of the molecule is always smaller than the observed value. This means that a surface-directed dipole moment exists. Generally, the metal-facing dipole layer is generated at the metal/organic interface by the push-back effect. Because the present dipole is in the opposite direction, it is most likely generated by the chemical interaction between the electrode and the phosphonic acid anchor group.

3.2. Ionization energy of HCM

Finally, we consider the ionization energy of the HCMs. Because of weak intermolecular interactions, the energy levels (ionization energy and electron affinity) of organic semiconductors (in the solid phase) are primarily determined by those of the isolated molecules (in the gas phase) and perturbed by the polarization energy accounting for the interaction between the ion and the surrounding neutral molecules.[72] The polarization energy can be further divided into electrostatic and electronic polarization contributions.[73–75] We have demonstrated that the

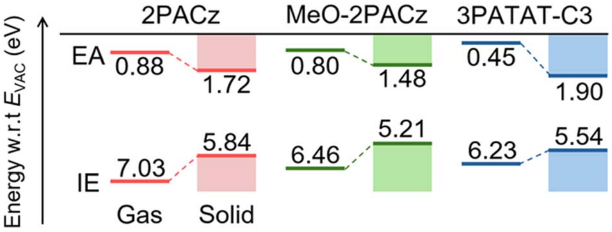

Fig. 9 Ionization energy (HOMO level) and electron affinity (LUMO level) of HCMs in the gas and solid phases.

Table 3 Comparison of electrostatic energy, electronic polarization energy, and molecular density of the HCMs

HCM	Electrostatic energy [eV]	Polarization energy [eV]	Surface density [10^{13} cm^{-2}]
2PACz	0.17	1.01	7.10[a]
MeO-2PACz	0.28	0.96	7.10
3PATAT-C3	−0.38	1.07	1.04

[a] The molecular density of 2PACz is assumed to be the same as that of MeO-2PACz.

electronic polarization energy and the electrostatic energy can be experimentally measured from the ionization energy and the electron affinity.[76–78] In the present HCMs, the electrostatic energy is determined by the molecular orientation,[76,79] whereas the electronic polarization energy is determined by the molecular density.[80]

Fig. 9 shows the ionization energies and the electron affinities of the HCMs in the gas and solid phases. The solid-state values are taken from the present measurements shown in Fig. 2. The gas-phase values are derived from the total energy difference between the ionic and neutral molecules with the geometry of the neutral molecule (assuming a vertical transition) using B3LYP/6-31G(d). The observed ionization energy and electron affinity in the solid are constantly decreased by about 1 eV from the corresponding values in the gas phase. The polarization energy of 1 eV is typical for organic semiconductors,[81] confirming that the ionization energy of HCMs is primarily the property of the isolated HCM molecule. Table 3 shows the calculated electrostatic energy and polarization energy according to eqn (S2). The difference in ionization energy between the gas and solid phases is larger for 2PACz and MeO-2PACz than for 3PATAT-C3. This difference is attributed to the lower electrostatic energy of 3PATAT-C3 (Table 3), which can be explained by the face-on molecular orientation of 3PATAT-C3.[75,76]

4. Conclusion

We examined the hole collection efficiencies of HCMs from the perspective of energy level alignment at electrode/HCM/perovskite interfaces. To describe HCM-dependent photovoltaic performance, we established a universal model in which the HCM/perovskite interface is treated as a semiconductor heterojunction, whereas the electrode/HCM interface is described in terms of interface dipole formation at a conventional metal/organic interface. In this model, the work function difference between the HCM and perovskite determines the direction and magnitude of band bending in the perovskite ($\Delta\Phi$), whereas the ionization energy difference sets the interfacial energy barrier (ΔE_V).

Based on energy parameters determined by UPS/LEIPS, the model consistently explains the performance trends for representative carbazole-based HCMs (2PACz, MeO-2PACz, and 3PATAT-C3) combined with four perovskites ($Cs_{0.05}FA_{0.80}MA_{0.15}PbI_{2.75}Br_{0.25}$, $Cs_{0.05}FA_{0.73}MA_{0.22}PbI_{2.31}Br_{0.69}$, $MAPbI_3$, and $FASnI_3$). We further tested the model using literature data on a broad set of non-carbazole HCMs, and found that the predicted hole collection favorability, evaluated from $\Delta\Phi$ and ΔE_V, correlates well with reported photovoltaic performance across diverse HCM/perovskite combinations. These results demonstrate that an energetically favorable alignment, namely, negligible interfacial hole barriers together with upward band bending on the perovskite side, is a necessary condition for efficient hole collection, in which other factors, such as wettability, film uniformity, and defect passivation, can provide additional improvements.

We also investigated the origin of the energy parameters required by this model in order to provide guidelines for the selection and fabrication of HCM materials. UPS measurements indicated that the work function of the HCM is primarily determined by that of the electrode, which is modified by the dipole layer created by the HCM layer. We emphasized the effect of the oft-overlooked electrode work function. The magnitude of the dipole layer is determined by the molecular orientation and the dipole moment as expressed by the Helmholtz equation, and confirmed by the molecular orientations determined by UPS and MAES in combination with the calculated molecular dipole moment. On the other hand, the ionization energy of HCM from the ionization energy of each molecule, which is modified by the polarization energy. Through these efforts, we were able to understand all four energy parameters of HCM required for our new model. Overall, the present study enabled the prediction of photovoltaic performance of HCM materials and provided guidelines for the design and selection of HCMs for the hole-collecting layer of high-efficiency perovskite solar cells.

5. Experimental methods

2PACz and MeO-2PACz films were prepared at the University of Electro-Communications. A 1 mM solution of 2PACz (or MeO-2PACz) in isopropyl alcohol (IPA) was spin-coated onto an indium tin oxide-coated (ITO) glass plate. After annealing at 100 °C for 10 minutes in a nitrogen atmosphere, 2PACz (or MeO-2PACz) molecules that were not adsorbed on ITO were washed off with IPA, and a second annealing was performed at 100 °C for 1 minute. 3PATAT-C3 and mixed composition perovskite ($Cs_{0.05}FA_{0.80}MA_{0.15}PbI_{2.75}Br_{0.25}$) films were prepared at Kyoto University, the details of which are described in ref. 26 and 39. 3PATAT-C3 samples were prepared on ITO and F-doped tin oxide-coated (FTO) glass plates. The perovskite sample was prepared on the ITO glass plate and HCMs coated on ITO. These sample films were kept in a nitrogen atmosphere and transported to Chiba University for electron spectroscopy measurements.

Ultraviolet photoelectron spectroscopy (UPS), metastable atom electron spectroscopy (MAES), and low-energy inverse photoelectron spectroscopy (LEIPS)[40,82] were performed at Chiba University. For UPS and MAES measurements, the samples were introduced into a measurement chamber at a pressure of 3.2×10^{-8} Pa. For UPS measurement, He I (photon energy of 21.22 eV) radiation from a He discharge lamp (VG Microtech, UVL-Hi and SPECS, UVS 10/35) were used to measure electrodes and electrode/HCMs, and electrode/perovskite, respectively.) was incident on the sample at an angle of 45°, and photoelectrons emitted normal to the samples were analyzed by an electron energy analyzer (SPECS, PHOIBOS 100). Vacuum levels were determined from the secondary electron cut-off measured by applying a -5 V bias voltage to the sample. The valence band spectra were measured without the bias voltage.

For MAES measurement, metastable He atoms (He*: 19.82 eV in excitation energy) were used as the excitation source. The measurement was performed at a He* incidence angle of 0° and an electron detection angle of 60°. A bias voltage of -1 V was applied to the sample. The pressure during the measurement was 2.0×10^{-7} Pa. Peak positions in the UPS and MAES spectra were determined from the minimum of the second derivative of the spectra after smoothing four times (68 points) using the quadratic Savitzky–Golay method.

After the UPS and MAES measurements, the LEIPS measurement of the electrodes and the perovskite sample was carried out in the same vacuum chamber as the UPS and MAES measurements. HCM samples were exposed to the atmosphere once and introduced into another vacuum chamber at a pressure of 1.5×10^{-7} Pa to measure LEIPS. Details of the LEIPS setup and measurement are described elsewhere.[50,83] For HCM samples, a Cs–Te photomultiplier tube (Hamamatsu Photonics, R821) was used to avoid electron-excited fluorescence.[50] For the other samples, a bialkali photomultiplier (Hamamatsu Photonics, R585s) was employed. Band-pass filters with center wavelengths of 285 nm and 260 nm were used for HCMs and the other materials, respectively. The vacuum level was obtained from the peak energy of the first derivative of the low-energy electron transmission (LEET). Electron affinity was determined as the onset of the LEIPS spectrum with respect to the vacuum level.

Author contributions

A. A. carried out the MAES, UPS and LEIPS measurements, analyzed data including the theoretical calculations and proposed the original concept of the model under the supervision of H. Y. A. A. and H. Y. jointly developed the model and wrote the manuscript. M. A. T., A. W. prepared 3PATAT-C3 and perovsktie samples coated on ITO and FTO, fabricated the solar cells and conducted current–voltage measurements. G. K. and S. H. provided 2PACz and MeO-2PACz samples. All authors contributed to the discussion of the results and approved the final manuscript.

Conflicts of interest

There are no conflicts to declare.

Data availability

The data that support the findings of this study are available from the corresponding author upon reasonable request.

Supplementary information (SI): details on the determination of the energy levels of perovskites, the previous models shown in Fig. 1, the hole-collecting layer/perovskite interface energy levels for $MAPbI_3$ and $FASnI_3$ based on the proposed model, validation of the general applicability of the proposed energy-level alignment model, the principles of molecular orientation analysis using UPS and MAES, and calculations of the electrostatic and polarization energies. See DOI: https://doi.org/10.1039/d5ta04749h.

Acknowledgements

This work was supported by JST–MIRAI (JPMJMI22E2) and JSPS-KAKENHI through a Grant-in-Aid for Scientific Research (A) (JP24H00446) and a Grant-in-Aid for Transformative Research Areas (A) (JP23H03939). A. A. thanks a Grant-in-Aid for JSPS Fellows (JP25KJ0718). A. W. and M. A. T. acknowledge support from JSPS KAKENHI Grant-in-Aid for Scientific Research (A) (JP24H00481) and (B) (JP24K01571), respectively.

References

1 L. Dou, Y. (Micheal) Yang, J. You, Z. Hong, W.-H. Chang, G. Li and Y. Yang, Solution-processed hybrid perovskite photodetectors with high detectivity, *Nat. Commun.*, 2014, **5**, 5404.

2 W. Nie, H. Tsai, R. Asadpour, J.-C. Blancon, A. J. Neukirch, G. Gupta, J. J. Crochet, M. Chhowalla, S. Tretiak, M. A. Alam, H.-L. Wang and A. D. Mohite, High-efficiency solution-processed perovskite solar cells with millimeter-scale grains, *Science*, 2015, **347**, 522–525.

3 NREL, *Best Research-Cell Efficiencies*, https://www.nrel.gov/pv/cell-efficiency.html, accessed January 2026.

4 H. Zhang and N.-G. Park, Progress and issues in p-i-n type perovskite solar cells, *DeCarbon*, 2024, **3**, 100025.

5 H. Kim, K.-G. Lim and T.-W. Lee, Planar heterojunction organometal halide perovskite solar cells: roles of interfacial layers, *Energy Environ. Sci.*, 2016, **9**, 12–30.

6 E. Köhnen, M. Jošt, A. B. Morales-Vilches, P. Tockhorn, A. Al-Ashouri, B. Macco, L. Kegelmann, L. Korte, B. Rech, R. Schlatmann, B. Stannowski and S. Albrecht, Highly efficient monolithic perovskite silicon tandem solar cells: analyzing the influence of current mismatch on device performance, *Sustain. Energy Fuels*, 2019, **3**, 1995–2005.

7 H. Tran, S. D. H. Naqvi, K. Kim, A. Lee, S. Oh, Y. Siddique, A. Ullah, S. S. F. Ali, M. Park, S. Hong, S. Ahn, J. Gwak and I. Jeong, Triple-halide wide-bandgap perovskites tailored *via* facile organic halide treatment for high-performance perovskite/Cu(In,Ga)Se_2 tandem solar cells, *Chem. Eng. J.*, 2023, **476**, 146825.

8 E. A. Nyiekaa, T. A. Aika, P. E. Orukpe, C. E. Akhabue and E. Danladi, Development on inverted perovskite solar cells: A review, *Heliyon*, 2024, **10**, e24689.

9 J.-Y. Jeng, Y.-F. Chiang, M.-H. Lee, S.-R. Peng, T.-F. Guo, P. Chen and T.-C. Wen, $CH_3NH_3PbI_3$ perovskite/fullerene planar-heterojunction hybrid solar cells, *Adv. Mater.*, 2013, **25**, 3727–3732.

10 J. You, Z. Hong, Y. (Michael) Yang, Q. Chen, M. Cai, T.-B. Song, C.-C. Chen, S. Lu, Y. Liu, H. Zhou and Y. Yang, Low-temperature solution-processed perovskite solar cells with high efficiency and flexibility, *ACS Nano*, 2014, **8**, 1674–1680.

11 J. H. Heo, S. H. Im, J. H. Noh, T. N. Mandal, C.-S. Lim, J. A. Chang, Y. H. Lee, H. Kim, A. Sarkar, Md. K. Nazeeruddin, M. Grätzel and S. I. Seok, Efficient inorganic-organic hybrid heterojunction solar cells containing perovskite compound and polymeric hole conductors, *Nat. Photonics*, 2013, **7**, 486–491.

12 B. Zhao, X. Huang, S. Chung, M. Zhang, Y. Zhong, A. Liang, Z. Zhao, C. Zhu, J. Zhao, S. Kim, J. Kim, M. Wang, S. Chen, K. Cho, Y. Wang and Z. Kan, Hole-selective-molecule doping improves the layer thickness tolerance of PEDOT:PSS for efficient organic solar cells, *eScience*, 2025, **5**, 100305.

13 N. Yaghoobi Nia, M. Méndez, B. Paci, A. Generosi, A. Di Carlo and E. Palomares, Analysis of the efficiency losses in hybrid perovskite/PTAA solar cells with different molecular weights: morphology *versus* kinetics, *ACS Appl. Energy Mater.*, 2020, **3**, 6853–6859.

14 S. H. Chang, K.-F. Lin, K. Y. Chiu, C.-L. Tsai, H.-M. Cheng, S.-C. Yeh, W.-T. Wu, W.-N. Chen, C.-T. Chen, S.-H. Chen and C.-G. Wu, Improving the efficiency of $CH_3NH_3PbI_3$ based photovoltaics by tuning the work function of the PEDOT:PSS hole transport layer, *Sol. Energy*, 2015, **122**, 892–899.

15 A. Magomedov, A. Al-Ashouri, E. Kasparavičius, S. Strazdaite, G. Niaura, M. Jošt, T. Malinauskas, S. Albrecht and V. Getautis, Self-assembled hole transporting monolayer for highly efficient perovskite solar cells, *Adv. Energy Mater.*, 2018, **8**, 1801892.

16 A. Al-Ashouri, E. Köhnen, B. Li, A. Magomedov, H. Hempel, P. Caprioglio, J. A. Márquez, A. B. Morales-Vilches, E. Kasparavicius, J. A. Smith, N. Phung, D. Menzel, M. Grischek, L. Kegelmann, D. Skroblin, C. Gollwitzer, T. Malinauskas, M. Jošt, G. Matič, B. Rech, R. Schlatmann, M. Topič, L. Korte, A. Abate, B. Stannowski, D. Neher, M. Stolterfoht, T. Unold, V. Getautis and S. Albrecht, Monolithic perovskite/silicon tandem solar cell with >29% efficiency by enhanced hole extraction, *Science*, 2020, **370**, 1300–1309.

17 P. J. Hotchkiss, S. C. Jones, S. A. Paniagua, A. Sharma, B. Kippelen, N. R. Armstrong and S. R. Marder, The modification of indium tin oxide with phosphonic acids: mechanism of binding, tuning of surface properties, and potential for use in organic electronic applications, *Acc. Chem. Res.*, 2012, **45**, 337–346.

18 E. Li, E. Bi, Y. Wu, W. Zhang, L. Li, H. Chen, L. Han, H. Tian and W.-H. Zhu, Synergistic coassembly of highly wettable and uniform hole-extraction monolayers for scaling-up perovskite solar cells, *Adv. Funct. Mater.*, 2020, **30**, 1909509.

19 T. Wu, S. Mariotti, P. Ji, L. K. Ono, T. Guo, I.-N. Rabehi, S. Yuan, J. Zhang, C. Ding, Z. Guo and Y. Qi, Self-assembled monolayer hole-selective contact for up-scalable and cost-effective inverted perovskite solar cells, *Adv. Funct. Mater.*, 2024, **34**, 2316500.

20 H. Chen, C. Liu, J. Xu, A. Maxwell, W. Zhou, Y. Yang, Q. Zhou, A. S. R. Bati, H. Wan, Z. Wang, L. Zeng, J. Wang, P. Serles, Y. Liu, S. Teale, Y. Liu, M. I. Saidaminov, M. Li, N. Rolston, S. Hoogland, T. Filleter, M. G. Kanatzidis, B. Chen, Z. Ning and E. H. Sargent, Improved charge extraction in inverted perovskite solar cells with dual-site-binding ligands, *Science*, 2024, **384**, 189–193.

21 E. Ugur, A. A. Said, P. Dally, S. Zhang, C. E. Petoukhoff, D. Rosas-Villalva, S. Zhumagali, B. K. Yildirim, A. Razzaq, S. Sarwade, A. Yazmaciyan, D. Baran, F. Laquai, C. Değer, I. Yavuz, T. G. Allen, E. Aydin and S. De Wolf, Enhanced cation interaction in perovskites for efficient tandem solar cells with silicon, *Science*, 2024, **385**, 533–538.

22 P. Han and Y. Zhang, Recent advances in carbazole-based self-assembled monolayer for solution-processed optoelectronic devices, *Adv. Mater.*, 2024, **36**, 2405630.

23 K. Guo, H. Tang, L. Han, R. Qi, H. Yan, G. Gao, W. Lv, M. Li, J. Xia, B. Cai, G. Xing, R. Chen and G. Wu, Self-assembled monolayer: revolutionizing p-i-n perovskite solar cells, *ACS Energy Lett.*, 2025, **10**, 4882–4910.

24 G. Kapil, T. Bessho, Y. Sanehira, S. R. Sahamir, M. Chen, A. K. Baranwal, D. Liu, Y. Sono, D. Hirotani, D. Nomura, K. Nishimura, M. A. Kamarudin, Q. Shen, H. Segawa and S. Hayase, Tin–lead perovskite solar cells fabricated on hole selective monolayers, *ACS Energy Lett.*, 2022, **7**, 966–974.

25 A. Al-Ashouri, A. Magomedov, M. Roß, M. Jošt, M. Talaikis, G. Chistiakova, T. Bertram, J. A. Márquez, E. Köhnen, E. Kasparavičius, S. Levcenco, L. Gil-Escrig, C. J. Hages, R. Schlatmann, B. Rech, T. Malinauskas, T. Unold, C. A. Kaufmann, L. Korte, G. Niaura, V. Getautis and S. Albrecht, Conformal monolayer contacts with lossless interfaces for perovskite single junction and monolithic tandem solar cells, *Energy Environ. Sci.*, 2019, **12**, 3356–3369.

26 M. A. Truong, T. Funasaki, L. Ueberricke, W. Nojo, R. Murdey, T. Yamada, S. Hu, A. Akatsuka, N. Sekiguchi, S. Hira, L. Xie, T. Nakamura, N. Shioya, D. Kan, Y. Tsuji, S. Iikubo, H. Yoshida, Y. Shimakawa, T. Hasegawa, Y. Kanemitsu, T. Suzuki and A. Wakamiya, Tripodal triazatruxene derivative as a face-on oriented hole-collecting monolayer for efficient and stable inverted perovskite solar cells, *J. Am. Chem. Soc.*, 2023, **145**, 7528–7539.

27 I. Levine, A. Al-Ashouri, A. Musiienko, H. Hempel, A. Magomedov, A. Drevilkauskaite, V. Getautis, D. Menzel, K. Hinrichs, T. Unold, S. Albrecht and T. Dittrich, Charge transfer rates and electron trapping at buried interfaces of perovskite solar cells, *Joule*, 2021, **5**, 2915–2933.

28 F. J. Angus, W. K. Yiu, H. Mo, T. L. Leung, M. U. Ali, Y. Li, J. Wang, A. W. Y. Ho-Baillie, G. Cooke, A. B. Djurišić and P. Docampo, Understanding the impact of SAM Fermi levels on high efficiency p-i-n perovskite solar cells, *J. Phys. Chem. Lett.*, 2024, **15**, 10686–10695.

29 N. Sekiguchi, Y. Tsuji, M. A. Truong, A. Wakamiya and S. Iikubo, Optimization of band alignment by organic molecules for perovskite solar cells, *J. Phys. Chem. C*, 2025, **129**, 8500–8508.

30 Q. Liao, Y. Wang, Z. Zhang, K. Yang, Y. Shi, K. Feng, B. Li, J. Huang, P. Gao and X. Guo, Self-assembled donor-acceptor hole contacts for inverted perovskite solar cells with an efficiency approaching 22%: the impact of anchoring groups, *J. Energy Chem.*, 2022, **68**, 87–95.

31 J. Sun, C. Shou, J. Sun, X. Wang, Z. Yang, Y. Chen, J. Wu, W. Yang, H. Long, Z. Ying, X. Yang, J. Sheng, B. Yan and J. Ye, NiO_X-seeded self-assembled monolayers as highly hole-selective passivating contacts for efficient inverted perovskite solar cells, *Sol. RRL*, 2021, **5**, 2100663.

32 B. Li, J. Deng, J. A. Smith, P. Caprioglio, K. Ji, D. Luo, J. D. McGettrick, K. D. G. I. Jayawardena, R. C. Kilbride, A. Ren, S. Hinder, J. Bi, T. Webb, I. Marko, X. Liu, Y. Xiang, J. Reding, H. Li, S. Du, D. G. Lidzey, S. D. Stranks, T. Watson, S. Sweeney, H. J. Snaith, S. R. P. Silva and W. Zhang, Suppressing interfacial recombination with a strong-interaction surface modulator for efficient inverted perovskite solar cells, *Adv. Energy Mater.*, 2022, **12**, 2202868.

33 G. Wang, J. Zheng, W. Duan, J. Yang, M. A. Mahmud, Q. Lian, S. Tang, C. Liao, J. Bing, J. Yi, T. L. Leung, X. Cui, H. Chen, F. Jiang, Y. Huang, A. Lambertz, M. Jankovec, M. Topič, S. Bremner, Y.-Z. Zhang, C. Cheng, K. Ding and A. Ho-Baillie, Molecular engineering of hole-selective layer for high band gap perovskites for highly efficient and stable perovskite–silicon tandem solar cells, *Joule*, 2023, **7**, 2583–2594.

34 Y. Guo, S. Du, W. Chen, H. Zhou, G. Chen, S. Wang, Z. Yu, X. Hu, F. Yao, C. Li, W. Ke and G. Fang, Contact potential homogenization *via* buried interface engineering enables high-performance wide-bandgap perovskite photovoltaics, *Adv. Funct. Mater.*, 2025, **35**, 2500168.

35 A. Ullah, K. H. Park, Y. Lee, S. Park, A. B. Faheem, H. D. Nguyen, Y. Siddique, K.-K. Lee, Y. Jo, C.-H. Han, S. Ahn, I. Jeong, S. Cho, B. Kim, Y. S. Park and S. Hong, Versatile hole selective molecules containing a series of heteroatoms as self-assembled monolayers for efficient p-i-n perovskite and organic solar cells, *Adv. Funct. Mater.*, 2022, **32**, 2208793.

36 H. Bi, J. Liu, R. Beresneviciute, D. Tavgeniene, Z. Zhang, L. Wang, G. Kapil, C. Ding, S. R. Sahamir, Y. Sanehira, A. K. Baranwal, T. Kitamura, D. Wang, Y. Wei, Y. Yang, D.-W. Kang, S. Grigalevicius, Q. Shen and S. Hayase, Efficiency enhancement of wide bandgap lead perovskite solar cells with PTAA surface-passivated with monomolecular layer from the viewpoint of PTAA band bending, *ACS Appl. Mater. Interfaces*, 2023, **15**, 41549–41559.

37 Q. Tan, Z. Li, G. Luo, X. Zhang, B. Che, G. Chen, H. Gao, D. He, G. Ma, J. Wang, J. Xiu, H. Yi, T. Chen and Z. He, Inverted perovskite solar cells using dimethylacridine-based dopants, *Nature*, 2023, **620**, 545–551.

38 H. Bi, J. Liu, Z. Zhang, L. Wang, R. Beresneviciute, D. Tavgeniene, G. Kapil, C. Ding, A. K. Baranwal, S. R. Sahamir, Y. Sanehira, H. Segawa, S. Grigalevicius, Q. Shen and S. Hayase, All-perovskite tandem solar cells approach 26.5% efficiency by employing wide bandgap lead perovskite solar cells with new monomolecular hole transport layer, *ACS Energy Lett.*, 2023, **8**, 3852–3859.

39 M. Ozaki, Y. Ishikura, M. A. Truong, J. Liu, I. Okada, T. Tanabe, S. Sekimoto, T. Ohtsuki, Y. Murata, R. Murdey and A. Wakamiya, Iodine-rich mixed composition perovskites optimised for tin(IV) oxide transport layers: the influence of halide ion ratio, annealing time, and ambient air aging on solar cell performance, *J. Mater. Chem. A*, 2019, **7**, 16947–16953.

40 H. Yoshida, Near-ultraviolet inverse photoemission spectroscopy using ultra-low energy electrons, *Chem. Phys. Lett.*, 2012, **539–540**, 180–185.

41 S. M. Sze and K. K. Ng, *Physics of Semiconductor Devices*, John Wiley & Sons, Inc., Hoboken, NJ, 3rd edn, 2012.

42 H. Ishii, K. Sugiyama, E. Ito and K. Seki, Energy level alignment and interfacial electronic structures at organic/metal and organic/organic interfaces, *Adv. Mater.*, 1999, **11**, 605–625.

43 G. Qu, S. Cai, Y. Qiao, D. Wang, S. Gong, D. Khan, Y. Wang, K. Jiang, Q. Chen, L. Zhang, Y.-G. Wang, X. Chen, A. K.-Y. Jen and Z.-X. Xu, Conjugated linker-boosted self-assembled monolayer molecule for inverted perovskite solar cells, *Joule*, 2024, **8**, 2123–2134.

44 A. Ullah, K. H. Park, H. D. Nguyen, Y. Siddique, S. F. A. Shah, H. Tran, S. Park, S. I. Lee, K.-K. Lee, C.-H. Han, K. Kim, S. Ahn, I. Jeong, Y. S. Park and S. Hong, Novel phenothiazine-based self-assembled monolayer as a hole selective contact for highly efficient and stable p-i-n perovskite solar cells, *Adv. Energy Mater.*, 2022, **12**, 2103175.

45 M. Liu, M. Li, Y. Li, Y. An, Z. Yao, B. Fan, F. Qi, K. Liu, H.-L. Yip, F. R. Lin and A. K.-Y. Jen, Defect-passivating and stable benzothiophene-based self-assembled monolayer for high-performance inverted perovskite solar cells, *Adv. Energy Mater.*, 2024, **14**, 2303742.

46 R. He, W. Wang, Z. Yi, F. Lang, C. Chen, J. Luo, J. Zhu, J. Thiesbrummel, S. Shah, K. Wei, Y. Luo, C. Wang, H. Lai, H. Huang, J. Zhou, B. Zou, X. Yin, S. Ren, X. Hao, L. Wu, J. Zhang, J. Zhang, M. Stolterfoht, F. Fu, W. Tang and D. Zhao, Improving interface quality for 1-cm^2 all-perovskite tandem solar cells, *Nature*, 2023, **618**, 80–86.

47 J. Wu, P. Yan, D. Yang, H. Guan, S. Yang, X. Cao, X. Liao, P. Ding, H. Sun and Z. Ge, Bisphosphonate-anchored self-assembled molecules with larger dipole moments for

efficient inverted perovskite solar cells with excellent stability, *Adv. Mater.*, 2024, **36**, 2401537.

48 K. Zhao, Q. Liu, L. Yao, C. Değer, J. Shen, X. Zhang, P. Shi, Y. Tian, Y. Luo, J. Xu, J. Zhou, D. Jin, S. Wang, W. Fan, S. Zhang, S. Chu, X. Wang, L. Tian, R. Liu, L. Zhang, I. Yavuz, H. Wang, D. Yang, R. Wang and J. Xue, *peri*-Fused polyaromatic molecular contacts for perovskite solar cells, *Nature*, 2024, **632**, 301–306.

49 S. Pradhan, H. Bì, G. Kapil, A. Akatsuka, A. K. Baranwal, D. Wang, D. Liu, S. Shaban, T. Kitamura, S. R. Sahamir, Y. Fujiwara, J. Liu, H. Segawa, H. Yoshida, Q. Shen and S. Hayase, Interfacial dipole engineering *via* boronic acid-based self-assembled monolayers in inverted tin–lead perovskite solar cells with ideal band gap, *ACS Energy Lett.*, 2025, **10**, 4983–4994.

50 A. Akatsuka, M. Miura, G. Kapil, S. Hayase and H. Yoshida, Direct measurement of electron affinity of carbazole-based self-assembled monolayer used as hole-selective layer in high-efficiency perovskite solar cells, *Appl. Phys. Lett.*, 2024, **124**, 241603.

51 J. Endres, D. A. Egger, M. Kulbak, R. A. Kerner, L. Zhao, S. H. Silver, G. Hodes, B. P. Rand, D. Cahen, L. Kronik and A. Kahn, Valence and conduction band densities of states of metal halide perovskites: a combined experimental–theoretical study, *J. Phys. Chem. Lett.*, 2016, **7**, 2722–2729.

52 F. Zu, P. Amsalem, D. A. Egger, R. Wang, C. M. Wolff, H. Fang, M. A. Loi, D. Neher, L. Kronik, S. Duhm and N. Koch, Constructing the electronic structure of $CH_3NH_3PbI_3$ and $CH_3NH_3PbBr_3$ perovskite thin films from single-crystal band structure measurements, *J. Phys. Chem. Lett.*, 2019, **10**, 601–609.

53 A. Mirzehmet, T. Ohtsuka, S. A. A. Rahman, T. Yuyama, P. Krüger and H. Yoshida, Surface termination of solution-processed $CH_3NH_3PbI_3$ perovskite film examined using electron spectroscopies, *Adv. Mater.*, 2021, **33**, 2004981.

54 A. M. Boehm, T. Liu, S. M. Park, A. Abtahi and K. R. Graham, Influence of surface ligands on energetics at $FASnI_3/C_{60}$ interfaces and their impact on photovoltaic performance, *ACS Appl. Mater. Interfaces*, 2020, **12**, 5209–5218.

55 N. Hayashi, H. Ishii, Y. Ouchi and K. Seki, Examination of band bending at buckminsterfullerene (C_{60})/metal interfaces by the Kelvin probe method, *J. Appl. Phys.*, 2002, **92**, 3784–3793.

56 D. Cahen, Y. Rakita, D. A. Egger and A. Kahn, Surface defects control bulk carrier densities in polycrystalline Pb-halide perovskites, *Adv. Mater.*, 2024, **36**, 2407098.

57 D. Song, S. Narra, M.-Y. Li, J.-S. Lin and E. W.-G. Diau, Interfacial engineering with a hole-selective self-assembled monolayer for tin perovskite solar cells *via* a two-step fabrication, *ACS Energy Lett.*, 2021, **6**, 4179–4186.

58 B.-B. Yu, Z. Chen, Y. Zhu, Y. Wang, B. Han, G. Chen, X. Zhang, Z. Du and Z. He, Heterogeneous 2D/3D tin-halides perovskite solar cells with certified conversion efficiency breaking 14%, *Adv. Mater.*, 2021, **33**, 2102055.

59 Q. Tai, X. Guo, G. Tang, P. You, T.-W. Ng, D. Shen, J. Cao, C.-K. Liu, N. Wang, Y. Zhu, C.-S. Lee and F. Yan, Antioxidant grain passivation for air-stable tin-based perovskite solar cells, *Angew. Chem., Int. Ed.*, 2019, **58**, 806–810.

60 J. Zeng, Z. Liu, D. Wang, J. Wu, P. Zhu, Y. Bao, X. Guo, G. Qu, B. Hu, X. Wang, Y. Zhang, L. Yan, A. K.-Y. Jen and B. Xu, Small-molecule hole transport materials for >26% efficient inverted perovskite solar cells, *J. Am. Chem. Soc.*, 2025, **147**, 725–733.

61 Q. Liao, Y. Wang, X. Yao, M. Su, B. Li, H. Sun, J. Huang and X. Guo, A dual-functional conjugated polymer as an efficient hole-transporting layer for high-performance inverted perovskite solar cells, *ACS Appl. Mater. Interfaces*, 2021, **13**, 16744–16753.

62 Y. Kong, W. Wang, X. Guo, Y. Yang, T. Chen, X. Zheng, W. Yu, Y. Wang, M. Wang, Y. Hu, C. Xu, Y. Wu, D. Wang, Z. Hong, W. Tang, H. Chen and L. Zuo, Decoding the role of molecular orientation in conjugated self-assembled monolayers for high-performance binary organic photovoltaics approaching 20% efficiency, *Adv. Mater.*, 2025, **37**, 2501117.

63 I. Lange, S. Reiter, M. Pätzel, A. Zykov, A. Nefedov, J. Hildebrandt, S. Hecht, S. Kowarik, C. Wöll, G. Heimel and D. Neher, Tuning the work function of polar zinc oxide surfaces using modified phosphonic acid self-assembled monolayers, *Adv. Funct. Mater.*, 2014, **24**, 7014–7024.

64 L. Zhang, Y. Wang, J. Wen, Y. Huang, J. Gao, Y. Duan, S. Park, W. Shin, Z. Ma, M. Liu, S. W. Cho, Y. Park, Y. M. Jung, H. Lee, W. Liu and Y. Liu, Configurational isomerization-induced orientation switching: non-fused ring dipodal phosphonic acids as hole-extraction layers for efficient organic solar cells, *Angew. Chem., Int. Ed.*, 2024, **63**, e202408960.

65 S. Tanuma, C. J. Powell and D. R. Penn, Calculations of electron inelastic mean free paths. V. Data for 14 organic compounds over the 50–2000 eV range, *Surf. Interface Anal.*, 1994, **21**, 165–176.

66 Y. Harada, S. Masuda and H. Ozaki, Electron spectroscopy using metastable atoms as probes for solid surfaces, *Chem. Rev.*, 1997, **97**, 1897–1952.

67 A. Abdureyim, S. Kera, H. Setoyama, K. K. Okudaira, R. Suzuki, S. Masuda, N. Ueno and Y. Harada, Observation of outermost surface layer of 4-mercaptohydrocinnamic acid self-assembled film on Au(111) by Penning ionization electron spectroscopy, *Appl. Surf. Sci.*, 1999, **144–145**, 430–434.

68 S. Kera, Y. Yabuuchi, H. Yamane, H. Setoyama, K. K. Okudaira, A. Kahn and N. Ueno, Impact of an interface dipole layer on molecular level alignment at an organic-conductor interface studied by ultraviolet photoemission spectroscopy, *Phys. Rev. B:Condens. Matter Mater. Phys.*, 2004, **70**, 085304.

69 S. Kera, A. Abduaini, M. Aoki, K. K. Okudaira, N. Ueno, Y. Harada, Y. Shirota and T. Tsuzuki, Penning ionization electron spectroscopy of titanyl phthalocyanine ultrathin films: electronic state and molecular orientation, *J. Electron Spectrosc. Relat. Phenom.*, 1998, **88–91**, 885–889.

70 T. Aihara, S. A. Abd-Rahman and H. Yoshida, Metal screening effect on energy levels at metal/organic interface: precise determination of screening energy using photoelectron and inverse-photoelectron spectroscopies, *Phys. Rev. B*, 2021, **104**, 085305.

71 G. Heimel, L. Romaner, E. Zojer and J.-L. Brédas, Toward control of the metal–organic interfacial electronic structure in molecular electronics: a first-principles study on self-assembled monolayers of π-conjugated molecules on noble metals, *Nano Lett.*, 2007, **7**, 932–940.

72 F. Gutmann and L. E. Lyons, *Organic Semiconductors*, John Wiley & Sons, 1967.

73 P. J. Bounds and R. W. Munn, Polarization energy of a localized charge in a molecular crystal. II. Charge-quadrupole energy, *Chem. Phys.*, 1981, **59**, 41–45.

74 N. Sato, H. Inokuchi and E. A. Silinsh, Reevaluation of electronic polarization energies in organic molecular crystals, *Chem. Phys.*, 1987, **115**, 269–277.

75 B. J. Topham and Z. G. Soos, Ionization in organic thin films: electrostatic potential, electronic polarization, and dopants in pentacene films, *Phys. Rev. B:Condens. Matter Mater. Phys.*, 2011, **84**, 165405.

76 K. Yamada, S. Yanagisawa, T. Koganezawa, K. Mase, N. Sato and H. Yoshida, Impact of the molecular quadrupole moment on ionization energy and electron affinity of organic thin films: experimental determination of electrostatic potential and electronic polarization energies, *Phys. Rev. B*, 2018, **97**, 245206.

77 Y. Uemura, S. A. Abd-Rahman, S. Yanagisawa and H. Yoshida, Quantitative analysis of the electrostatic and electronic polarization energies in molecularly mixed films of organic semiconductors, *Phys. Rev. B*, 2020, **102**, 125302.

78 S. A. Abd-Rahman, T. Yamaguchi, S. Kera and H. Yoshida, Sample-shape dependent energy levels in organic semiconductors, *Phys. Rev. B*, 2022, **106**, 075303.

79 A. Sugie, W. Han, N. Shioya, T. Hasegawa and H. Yoshida, Structure-dependent electron affinities of perylene diimide-based acceptors, *J. Phys. Chem. C*, 2020, **124**, 9765–9773.

80 Y. Zhong, S. Izawa, K. Hashimoto, K. Tajima, T. Koganezawa and H. Yoshida, Crystallization-induced energy level change of [6,6]-phenyl-C_{61}-butyric acid methyl ester (PCBM) film: impact of electronic polarization energy, *J. Phys. Chem. C*, 2015, **119**, 23–28.

81 N. Sato, K. Seki and H. Inokuchi, Polarization energies of organic solids determined by ultraviolet photoelectron spectroscopy, *J. Chem. Soc., Faraday Trans. 2*, 1981, **77**, 1621–1633.

82 H. Yoshida, Principle and application of low energy inverse photoemission spectroscopy: A new method for measuring unoccupied states of organic semiconductors, *J. Electron Spectrosc. Relat. Phenom.*, 2015, **204**, 116–124.

83 H. Yoshida, Note: low energy inverse photoemission spectroscopy apparatus, *Rev. Sci. Instrum.*, 2014, **85**, 016101.